Investigation of the optical and dielectric properties of NaCu0.2Fe0.8-xMnxO2 (x = 0.4; 0.5; 0.6; 0.7) layered oxide materials

Ichrak Ben Slima, Karim Karoui, Kamel Khirouni, Abdelfattah Mahmoud, Frédéric Boschini, Abdallah Ben Rhaiem

Investigation of the optical and dielectric properties of $NaCu_{0.2}Fe_{0.8-x}Mn_xO_2$ (x = 0.4; 0.5; 0.6; 0.7) layered oxide materials

Ichrak Ben Slima[a], Karim Karoui [a,d], Kamel Khirouni[b], Abdelfattah Mahmoud[c], Frédéric Boschini [c], Abdallah Ben Rhaiem[a,*]

[a] Laboratory LaSCOM, University of Sfax, BP1171, 3000, Sfax, Tunisia

[b]Laboratory of Physics of Materials and Nanomaterials applied to Environement, Faculty of Sciences of Gabès, University of Gabès, Tunisia.

[c] GREENMAT, CESAM, Institute of Chemistry B6, University of Liège, 4000 Liège, Belgium

[d] GREMAN UMR 7347-CNRS, CEA, INSACVL, University of Tours, Blois, France

*Corresponding author: abdallahrhaiem@yahoo.fr

Abstract

We prepared the compounds $NaCu_{0.2}Fe_{0.8-x}Mn_xO_2$ by the solid states method. The structural analysis confirmed that the samples crystallize in hexagonal system with R-3m space group. Fourier transform infrared spectroscopy shows vibrational modes of the compounds $NaCu_{0.2}Fe_{0.8-x}Mn_xO_2$ and proved the presence of the octahedral environment MO_6 (M= Cu, Fe, Mn) which validates the structural study. The investigation by UV-visible spectroscopy revealed a strong absorption of the prepared samples in the UV-visible range and allows extracting the band gap (2.8 eV $<E_g<$ 3 eV) which shows a small increase with manganese content and exhibits the samples semiconductor behavior. Additionally, the study of the real part of the dielectric permittivity using impedance spectroscopy demonstrated high dielectric constant at low frequency and suggested the existence of space charge polarization and dipolar polarization. However, the study of the imaginary part of the dielectric permittivity proved that the dipolar polarization may be masked due to the high ionic dc conductivity. Finally, modulus formalism indicated two relaxations attributed to the grain boundary and grain relaxations.

Key words: $NaCu_{0.2}Fe_{0.8-x}Mn_xO_2$ compounds, semiconductor, optical properties, dielectrical propreties.

I. Introduction

Sodium transition metal oxides Na_xMO_2, where M is a metal, have drawn extensive attention of researchers and whetted the widest interest in view of their layered structure and

their electrochemical performances which make them used as electrodes for sodium ion batteries, the best alternative for lithium ion batteries [1-3].

Although, these materials have continued to trigger significant scientific concern in terms of extracting more outstanding physical properties, such as optic and dielectric properties; to the best of our knowledge, the number of papers tackling these properties is scarce. It is noteworthy that Na_xMO_2 samples are characterized by the presence of the electronic configuration ([Ar] $3d^n$) of the transition metal allowing them to have specific electronic transitions, namely the d-d transitions on the metal site and the ligand to metal transition (e.g.: O to Cu) [4]. Additionally, they display a low band gap (e.g.: E_g ($NaFeO_2$ = 2.45eV)), a high dielectric constant (e.g.:($\varepsilon'(LiFeO_2)\approx 7.10^4$) and a low dielectric loss (e.g.: tgδ ($LiNi_{1/3}Co_{1/3}Mn_{(1/3)-x}Al_xO_2$) < 4)[5-7]… These properties open further fruitful lines of investigation and offer promising opportunities for these compounds to be invested in multiple scientific and technological applications including optoelectronics, gas absorber, gas sensor, medical treatment …. [8-11].

In our previous works, we attempted to determine the structural and electrical properties of $NaCu_{0.2}Fe_{0.8-x}Mn_xO_2$ samples (x= 0.4; 0.5; 0.6; 0.7) [12-13]. The obtained results revealed that these samples crystallize in the hexagonal system with the R-3m space group and possess a trace of Fe_2O_3 (fig. S1 and table S1 in the supporting information). Furthermore, the crystalline structure was handled. It is inferred that changing the Mn percentage, affects the lattice structure and switches it from O3 in samples whose x=0.4 and 0.5 to P3 for samples whose x=0.6 and 0.7. Indeed, in both structure types, the crystalline structure is formed by alternating sheets of $CuFeMnO_2$ sheets and NaO_2 sheets. The $CuFeMnO_2$ sheets are formed by $CuFeMnO_6$ octahedra, whereas the NaO_2 sheets are formed by either, NaO_6 octahedra in O3 structure, where sodium ions are located in octahedral sites, or NaO_6 prisms in P3 structure, where sodium ions are located in prismatic sites. Additionally, increasing Mn rate impacts the electrical conductivity and generates its increase as well as changes the conduction mechanism. These outstanding results constitute the basic impetus behind the attempts to identify further prominent features for these materials. From this perspective, the basic objective of the current research is to investigate the optic and dielectric properties of $NaCu_{0.2}Fe_{0.8-x}Mn_xO_2$ samples (x= 0.4; 0.5; 0.6; 0.7) and trace the evolution of optical and dielectric constants.

II. Materials and methods

Using the conventional solid state method, the $NaCu_{0.2}Fe_{0.8-x}Mn_xO_2$ compounds (x= 0.4; 0.5; 0.6; 0.7) were synthesized, where proportional ratios of Na_2CO_3 (Segma Aldrich, 99%), CuO (Segma Aldrich, 99%), Fe_2O_3 (Segma Aldrich, 99%) and Mn_2O_3 (Segma Aldrich, 99%) were mixed. Theses samples were subjugated to two thermal treatments at 500°C and 850°C for 16h and 24h, respectively, in air. The obtained samples were cooled in a glove box filled with argon. The samples were prepared following the equation:

$$Na_2CO_3 + (0.4)\ CuO + (0.8\text{-}x)\ Fe_2O_3 + x\ Mn_2O_3 + (0.1)\ O_2 \rightarrow 2\ NaCu_{0.2}Fe_{0.8-x}Mn_xO_2 + CO_2$$

We invested the X-Ray Diffraction on powder by 'Bruker D8 Discover Twin- Twin', at room temperature, with Cu K_α radiation (λ = 1.5406 Å, $10° \leq 2\theta \leq 80°$) in order to verify the purity of the prepared samples. [13]. In order to specify the composition of the prepared samples, Fourier transform infrared (FTIR) spectroscopy was performed on powder, at room temperature, using 'PERKIN-ELMER FT-IR Spectrum 1000'. Furthermore, to examine the optical properties, the UV-Visible spectroscopy at room temperature was invested using 'Shimadzu UV-3101 PC scanning spectrophotometer', in the wavelength range of 200–800 nm on a pellet of 0.5 mm of thickness. Finally, the dielectric properties were extracted using complex electric impedance spectroscopy with a 'Solartron SI 1260 impedance/gain phase analyzer' in the frequency range [10^{-1} to 10^6 Hz], at various temperatures. Measurements were undertaken on a pellet with a diameter of 8 mm and a thickness of 1mm.

III. Results and discussion

III.1. Vibrational analysis

The vibrational study was carried out using Fourier transmission infrared spectroscopy. FTIR analyses are depicted in fig 1.The FTIR graph revealed that the spectra of all samples exhibit very similar characteristics. The transmittance peaks appearing between 500 and 1400 cm^{-1} are characteristic of the prepared samples and describe the stretching and bonding of sodium and metal with oxygen in octahedral configuration, as portrayed in table 1. The peak at ≈1650cm^{-1} is associated to the absorbed water H_2O by the sample surface. This result proves the presence of the octahedral environment MO_6 (M= Cu, Fe, Mn) and confirms the structural study.

III.2. Optical properties

Fig 2 highlights the absorbance spectra associated with $NaCu_{0.2}Fe_{0.8-x}Mn_xO_2$ samples (x= 0.4; 0.5; 0.6; 0.7) obtained using UV-visible spectroscopy at room temperature. It suggests the presence of six absorption peaks. The maximum absorbance in the ultra-violet region of the electromagnetic spectrum (λ_1) may reflect an increase in the power of the light source. While the maximum absorbance, in visible region of the electromagnetic spectrum (λ_5), denotes the transition from the valence band to conduction band. Furthermore, these compounds exhibit a strong absorbance in the visible region referring to the existence of 3d transition metal. Indeed, relying on state of arts works, Mn^{3+} ($3d^4$), Fe^{3+} ($3d^5$) and Cu^{2+} ($3d^9$) absorb light in both ultra-violet and visible region. For Mn^{3+}, two absorption peaks are present at 317 nm and 519 nm, respectively; for Fe^{3+}, the absorption peaks are at 368 nm and 440 nm; and those for Cu^{2+} appear at 356 nm and 780 nm [22]. The deconvolution of the absorption spectrum shows peaks around these wavelengths. The observed shift can be attributed to the matrix absorption which complicated the deconvolution operation. These results lead us to attribute the wave length λ_2 to the absorption of Mn^{3+}. λ_3 can be assigned to the absorption of either Fe^{3+} or Cu^{2+}. Finally, λ_4 and λ_6 are attributed to the absorption of Fe^{3+} and Cu^{2+}, respectively. The transition associated with λ_2, λ_4 and λ_6 can be ascribed to transitions: $^5E_g \rightarrow {}^5T_{2g}$, $^6A_{1g}(S) \rightarrow {}^4T_{2g}(G)$ and $^2B_{1g} \rightarrow {}^2B_2$ of the Mn^{3+} , Fe^{3+} and Cu^{2+} ions; respectively. They are arranged in octahedral configuration with oxygen ions [23-27].

The strong absorption of $NaCu_{0.2}Fe_{0.8-x}Mn_xO_2$ samples in the UV-visible range is equally recorded in the absorbance spectra of $Mg_{0.6}Co_{0.2}Cu_{0.2}FeCrO_4$ spinel ferrites, where absorbance is near from the unity in the wavelength domain [200 nm- 800 nm]. This corroborates that our prepared samples can be invested in optoelectronic applications as well as in photo-catalysis materials and photovoltaic solar cells [28-29].

Additionly, samples absorbance is related to the absorption coefficient noted α. This coefficient describes the amount of electromagnetic wave absorbed by a material. It is determined through the following equation [30]:

$$\alpha = \frac{F(R)}{e} \qquad (1)$$

where $F(R) = \frac{(1-R)^2}{2R}$ is the Kubelka–Munk equation, R is the diffuse reflectance and e is the thikness of the sample.

Furthermore, the optical gap energy E_g was established using Tauc model [31]. The gap energy E_g and the absorption coefficient α are expressed in terms of the following relationship:

$$\alpha h\nu = B\,(h\nu - E_g)^{r} \qquad (2)$$

where B is a constant and r is a constant describing the nature of the optical transition between the valence band and the conduction band.

The value of the gap energy of $NaCu_{0.2}Fe_{0.8-x}Mn_xO_2$ samples was computed according to Tauc's plot $(\alpha h\nu)^2$ versus $(h\nu)$, as illustrated in Fig 3, through the intercept of the extrapolation of linear part of $(\alpha h\nu)^2$ with the $(h\nu)$ axis. Examining these results reveal that the values of direct band gap (table 2) vary in the range of 2.8e V< E_g < 3 eV, which confirms the semiconductor character of these compounds. Within this framework, the Mn substitution on Fe sites generates slowly the increase in E_g value. This may be accounted for by the fact that, when the Mn rate is higher than Fe rate, optical absorption in Mn based oxides is affected by d-d charge transfer between Mn ions at various sites and eg-eg transition of electron. Doping Mn at Fe sites inhibits the formation of new energy level for Fe which affected, therefore, the gap energy [32-33].

For instance, the gap energy of $NaCu_{0.2}Fe_{0.8-x}Mn_xO_2$ samples is close to those of $LiFeO_2$ (2.4 eV) and $NaFeO_2$ (2.17 eV). Thus, a study conducted by A.K. Tangra et al., unveiled the optical, magnetic and biocompatible applications of the $AFeO_2$ compounds to be used in medicine. These authors emphasized their efficiency and feasibility in terms of combating breast cancer cells. Therefore, our samples can be equally invested for medical treatment [34].

As the gap energy is attached to the absorption coefficient α, the extinction coefficient k is connected to it as well, via:

$$k = \frac{\alpha\lambda}{4\pi} \qquad (3)$$

Fig 4 presents the evolution of the extinction coefficient k as a function of the wavelength λ. all samples show an increase to a maximum value as λ increases then k drops when λ rises. The extinction coefficient k identifies a small value ranging between 10^{-7} and 10^{-6}, similarly to the recently studied $LiCoO_2$, indicating that $NaCu_{0.2}Fe_{0.8-x}Mn_xO_2$ samples

possess a low optical absorption loss when the incident light spreads through the crystal, which confirms their good transparency [35-37].

This result corroborate that the prepared samples correspond to outstanding materials in terms of photovoltaic solar cells and nonlinear optical applications [38-40].

Another intrinsic coefficient that needs to be investigated is refractive index n which describes the dispersion of the electromagnetic wave in a sample. It is calculated based on reflectivity R measurements following the equation below:

$$n = \frac{1+\sqrt{R}}{1-\sqrt{R}} \qquad (4)$$

As illustrated in fig 5, the refractive indices vary between 1.1 and 1.4, confirming extinction coefficient result and indicating the samples transparency. Noting that, sample whose x= 0.7 has the lower refractive index. Furthermore, the evolutions of this index present a minimum in the Ultra-Violet domain then it remain constant in the domain [400 nm – 700 nm], while in the domain [700 nm- 800 nm] a dispersion behavior appears.

This result is indicative that these compounds can act as good candidates in antireflection coatings with low refractive index [41].

Furthermore, these constants (n and k), when gathered, allow the study of the optical dielectric constant ε_{op} through the following relationships:

$$\varepsilon_{op} = \varepsilon' + j\varepsilon'' \qquad (5)$$

$$\varepsilon_{op}' = n^2 - k^2 \qquad (6)$$

$$\varepsilon_{op}'' = 2nk \qquad (7)$$

In this regard, the real part (ε_{op}') and the imaginary part (ε_{op}'') of the optical dielectric constant accounts for the slowing down of the light speed in the material and the free carriers' absorption of the associated radiation, respectively. Indeed, fig 6 and 7 trace the evolution of ε_{op}' and ε_{op}'' as a function of wavelength. First of all, the evolution of ε_{op}' and ε_{op}'' displays the same behavior of n and k, where ε_{op}' varies within the range 1.2- 1.8 and ε_{op}''ranges in the order 10^{-6} as the coefficient k. These results prove the transparency of the sample with very a small absorption loss.

In order to better and deeper investigate the optical area; the optical conductivity was invested to explore the optical transitions in a material. In other terms, the allowed interbond transitions [42]. The Optical conductivity is computed using the relation:

$$\sigma_{op} = \frac{\alpha n c}{4\pi} \qquad (8)$$

where c is the velocity of light and α is the absorption coefficient.

In this respect, the evolution of the optical conductivity vs. the photon energy is depicted in fig 8. In the visible domain, there is a maximum of conductivity, which implies that the photon energy induces more excited electrons at this domain. Such a result may be applied in opto-electronic devices, where our material seems to be a good alternative as an optical filter in the visible range to select specific frequencies [43]. It's worth noting that the optical conductivity σ_{op} decreases with the increase in Mn percentage. This can be ascribed to the increase of the optical gap which goes up with the rise of Mn amount.

The optical study shows that the gap energies of our compound remain higher than those of lithium-based compounds such as $LiCoO_2$ (2.15 eV) and $LiMnO_2$ (1.97 eV) [35] but they are lower than those of monophosphate materials such as the compound $NaCoPO_4$ in the three phases α, β and γ ($E_{g\alpha}$ = 4.08 , $E_{g\beta}$ = 4.35 and $E_{g\gamma}$ = 3.88 eV) [44]. In addition, our compounds are characterized by low extinction coefficient K (between 5 10^{-7} and 2.5 10^{-6}) which is of the same order of magnitude as that of pervoskyte compounds such as $[DMA]_2ZnCl_4$, $[DMA]_2ZnBr_4$ and $[DMA]_2CoCl_4$ (between 2 10^{-7} and 1.8 10^{-6}) [39]. These findings proved that these samples could be used in optoelectronic applications, active channel in FET devices, medical treatment and photovoltaic cells.

III.3. dielectric properties

In order to investigate the dynamic responses of the materials' constituents, it is quite informative to trace the evolution of their dielectric properties against the frequency [45]. However, the complex dielectric permittivity is expressed as follows:

$$\varepsilon_{el}^* = \varepsilon_{el}' + j\,\varepsilon_{el}'' \qquad (9)$$

where ε_{el}' is the real part of the dielectric permittivity indicating the ability of a material to be polarized or expressing its storage capacity and ε_{el}'' is the imaginary part of the dielectric permittivity corresponding to the energy loss in a sample [46].

Within this framework, the frequency dependence of the real part of the dielectric constant ε_{el}', at the temperature range [333 K- 453 K], of the $NaCu_{0.2}Fe_{0.8-x}Mn_xO_2$ samples (x= 0.4; 0.5; 0.6; 0.7) is illustrated in fig 9. Through analyzing these graphs, we can assert that in the low frequency region, the evolution of ε' is marked by a dispersion domain with a higher value of ε_{el}' ($\sim 10^7$); and in the high frequency region, it is characterized by a drop to a very small and constant value of ε_{el}' ($\sim 10^2$). The highly value of ε' at low frequencies can be assigned to the accumulation of the space charge at the interface and the high self ability of the permanent dipoles to be aligned along the electric field. On the other side, at high frequencies, as the applied field varies quickly, the permanent dipoles cannot follow it. Therefore, their response will be irrelevant and the variation of the dielectric constant ε_{el}' remains constant. Additionally, we notice that the real part of the dielectric permittivity is thermally activated since it increases as the temperature goes up. This refers basically to the fact that more dipoles are polarized and follow the field orientation [47]. This finding implies that the prepared samples are powerful candidates as active channels or dielectric gates to be used in FET devices [48].

To this extent, the influence of Mn substitution on the real part of the dielectric permittivity could be deduced. Fig 10 presents the evolution of ε_{el}', at high frequencies, at 333K. It confirms that ε' increases with the increase of Mn rate. This can be explained as follows; in an octahedral site, the oxidation states of Fe and Mn ions are Fe^{3+}/Fe^{4+} and Mn^{3+}/Mn^{4+}. Dopping Fe by Mn decreases the formation of defects and decreases the formation of Jahn Teller distortion of Mn^{4+} to Mn^{3+}. As a result, Mn dopping increases the oxidation state of Mn and therefore increases the dielectric constant as well as the electrical conductivity [49]. Noting that, the increase of the electrical conductivity by increasing Mn amount was proved in our previous work [13].

Furthermore, the evolution of the imaginary part of the dielectric permittivity ε_{el}'' against the frequency in log-log plot at various temperatures, plotted in fig 11, exhibits a linear response and reveals the absence of not only dielectric relaxations but also the dipolar relaxation. This can be accounted for in terms of the effect of the ionic dc conductivity (σ_{dc}), which obscures any relaxation process that might exist [50,13]. This proves that the conduction in these materials is very significant and therefore promising.

To further understand this phenomenon we used a simulation based on the Cole-Cole model following the equation [44]:

$$\varepsilon_{el}''(\omega) = \frac{\varepsilon_s - \varepsilon_\infty \left(\frac{\omega}{\omega_1}\right)^{(1-\alpha)} \sin\left(\frac{(1-\alpha)\Pi}{2}\right)}{1+2\left(\frac{\omega}{\omega_1}\right)^{1-\alpha} \cos\left(\frac{(1-\alpha)\Pi}{2}\right)+\left(\frac{\omega}{\omega_1}\right)^{2(1-\alpha)}} + \frac{\sigma_{dc}}{\varepsilon_0 \omega} \quad (10)$$

Where ε_∞ and ε_s are the high-frequency and static low frequency limits of the real permittivity, σ_{dc} is the DC conductivity and α is the Cole–Cole exponent.

The fit results of the frequency dependence of the imaginary part of the dielectric constant are shown in fig. S2 (supporting information). The conformity between theoretical and experimental data confirms that the cole-cole model describes well the relaxation process in these samples. Then, we can conclude the DC conductivity values and they are recapitulated in Table S2 (supporting information). The DC conductivity values varies between 10^{-6} and 10^{-3} $(\Omega\ cm)^{-1}$ and proves an increase as temperature increases. The high value of DC conductivity justifies the absence of dipolar relaxation.

Thus, the study of the electrical modulus seems to be the best tool to check the relaxation process in our samples. The imaginary part of the electric modulus M'' was calculated using the following expression [51]:

$$M'' = \frac{\varepsilon''}{\varepsilon'^2+\varepsilon''^2} \quad (11)$$

where ε' and $\varepsilon''$are the real and imaginary parts of the dielectric permittivity.

Fig 12 displays the imaginary part of modulus M'' against frequency at various temperatures. It's marked by the presence of two relaxation peaks. The first is at the neighborhood of 10^4 Hz and 10^5Hz, indicating the grain boundary relaxation. The second one appears at high frequencies, corresponding to the grain relaxation. At low frequencies, $M''(\omega)$ spectra are close to zero. This refers basically to the fact that modulus deletes the electrode effect [51]. By increasing Mn amount, the peaks shift towards high frequencies, which makes us unable to follow the relaxation in the sample whose x= 0.7 (fig 13). As a result, the relaxation time is reduced and the ionic transport becomes faster [52].This result suggests the enhancement of the conductivity which is corroborated in our previous work [13].

By increasing temperature, the relaxation peaks shift to high frequency, indicating that the relaxation process of conductivity is thermally activated. In order to pursue the evolution of the maximum frequency, characteristic of the relaxation of grains, the variation of Ln (ω_{max}) as a function of the inverse of temperature, is identified in fig 14. This variation follows the law of Arrhenius and the activation energies are recorded in table 3.

Then, the high dielectric constant of these materials (of the order of 10^6 at low frequency), which is of the same order of magnitude as that of the peroveskyte compounds $[DMA]_2ZnCl_4$, $[DMA]_2ZnBr_4$ and $[DMA]_2CoCl_4$ (between 10^6 and 5 10^6) [39], implies that these compounds could be a candidate in energy devices. Indeed, materials with high dielectric constant can be used as dielectric gate, gas absorber, gas sensors and super capacitors [53, 54].

Conclusion

$NaCu_{0.2}Fe_{0.8-x}Mn_xO_2$ compounds are preferred as electrodes for sodium ion batteries which highlight their significance in electrochemical applications. Consequently, it is crucial to investigate their optical and dielectric properties. $NaCu_{0.2}Fe_{0.8-x}Mn_xO_2$ samples were prepared using solid states method. Structural study revealed that these samples crystallize in hexagonal system with the R-3m space group. The vibrational study confirmed the structural study and showed the presence of all functional groups in the samples. Furthermore, the optical study was carried out using UV-Visible spectroscopy. It proved that the prepared samples stand for semiconductors whose gap energy varies between [2.8-3eV]. The increase in Mn percentage generates an increase in Eg value. We infer that the evolution of n and ε_{op}' vary in the range 1.2- 1.8. Likewise, ε_{op}'' and k are very low, vary in the order 10^{-6}. These findings proved that these samples could be used in optoelectronic applications, FET devices, medical treatment and photovoltaic cells. The dielectric study, using complex electric impedance spectroscopy, demonstrated that $NaCu_{0.2}Fe_{0.8-x}Mn_xO_2$ samples possess a high dielectric constant (ε_{el}' ($\sim 10^7$) at low frequency and ε_{el}' ($\sim 10^2$) at high frequency) and increase when Mn percentage rises. This proves the importance of these materials which can be used in several applications such as dielectric gates, gas absorbers, gas sensors and supercapacitors. The investigation of modulus formalism indicates two relaxations, namely grain boundary (around 10^4 Hz) and grain relaxation (around 10^6 Hz). These relaxations shift to higher frequencies by increasing the Mn rate, which generates a faster ionic transport.

References:

[1]. Kanwade, A., Gupta, S., Kankane, A., Tiwari, M. K., Srivastava, A., Satrughna, J. A. K., & Shirage, P. M. (2022). Transition metal oxides as a cathode for indispensable Na-ion batteries. *RSC advances*, *12*(36), 23284-23310. https://doi.org/10.1039/D2RA03601K

[2]. Kubota, K., Kumakura, S., Yoda, Y., Kuroki, K., & Komaba, S. (2018). Electrochemistry and solid-state chemistry of $NaMeO_2$ (Me= 3d transition metals). *Advanced Energy Materials*, *8*(17), 1703415. https://doi.org/10.1002/aenm.201703415

[3]. Singh, A. N., Islam, M., Meena, A., Faizan, M., Han, D., Bathula, C., & Nam, K. W. (2023). Unleashing the Potential of Sodium-Ion Batteries: Current State and Future Directions for Sustainable Energy Storage. *Advanced Functional Materials*, 2304617.DOI: 10.1002/adfm.202304617

[4]. Choudhury, D., Rivero, P., Meyers, D., Liu, X., Cao, Y., Middey, S., & Chakhalian, J. (2015). Anomalous charge and negative-charge-transfer insulating state in cuprate chain compound $KCuO_2$. *Physical Review B*, *92*(20), 201108. https://doi.org/10.1103/PhysRevB.92.201108

[5]. Singh, S., Tangra, A. K., & Lotey, G. S. (2018). Optical and luminescence properties of β-$NaFeO_2$ nanoparticles. *Electronic Materials Letters*, *14*(5), 594-598. https://doi.org/10.1007/s13391-018-0067-5

[6]. Rosaiah, P., & M Hussain, O. (2013). Synthesis, electrical and dielectrical properties of lithium iron oxide. *Advanced Materials Letters*, *4*(4), 288-295. https://dx.doi.org/10.5185/amlett.2012.8416

[7]. Murali, N., Margarette, S. J., & Veeraiah, V. (2017). Synthesis, dielectric, conductivity and magnetic studies of $LiNi_{1/3}Co_{1/3}Mn_{(1/3)-x}Al_xO_2$ (x= 0.0, 0.02, 0.04 and 0.06) for cathode materials of lithium-ion batteries. *Results in Physics*, *7*, 1379-1388. https://doi.org/10.1016/j.rinp.2017.02.037

[8]. Elamathi, R., Ramesh, R., Aravinthraj, M., Manivannan, M., Khan, F. L. A., Mphale, K., & Maaza, M. (2020). Investigation of structural and electrical properties of lithium cobalt oxide nanoparticles for optoelectronic applications. *Surfaces and Interfaces*, *20*, 100582. https://doi.org/10.1016/j.surfin.2020.100582

[9]. Liang, J. C., Yang, C. L., Wang, M. S., Ma, X. G., & Yi, Y. G. (2019). High mobility and photocatalytic properties of $NaXO_2$ (X= Co, Rh, Ir). *Vacuum*, *168*, 108824. https://doi.org/10.1016/j.vacuum.2019.108824

[10]. Triana, Y., Irkham, & Einaga, Y. (2022). Electrochemical oxidation behavior of nitrogen dioxide for gas detection using boron doped diamond electrodes. *Electroanalysis*, *34*(4), 752. DOI: 10.1002/elan.202100122

[11]. Singh, S., Kaur, J., Tovstolytkin, A., & Singh, G. (2019). Superparamagnetic β-$NaFeO_2$: a novel, efficient and biocompatible nanoparticles for treatment of cancer by nanohyperthermia. *Materials Research Express*, *6*(8), 0850a6. https://doi.org/10.1088/2053-1591/ab243e

[12]. Slima, I. B., Karoui, K., Mahmoud, A., Boschini, F., & Rhaiem, A. B. (2022). Structural, optical, electric and dielectric characterization of a $NaCu_{0.2}Fe_{0.3}Mn_{0.5}O_2$ compound. *RSC advances*, *12*(3), 1563-1570. https://doi.org/10.1039/D1RA08263A

[13]. Slima, I. B., Karoui, K., Mahmoud, A., Boschini, F., & Rhaiem, A. B. (2022). Effects of Mn doping on structural properties and conduction mechanism of $NaCu_{0.2}Fe_{0.8-x}Mn_xO_2$ (x= 0.4; 0.5; 0.6; 0.7) materials. *Journal of Alloys and Compounds*, *920*, 166002. https://doi.org/10.1016/j.jallcom.2022.166002.

[14]. Julien, C. M., Massot, M., & Poinsignon, C. (2004). Lattice vibrations of manganese oxides: Part I. Periodic structures. *Spectrochimica Acta Part A: Molecular and Biomolecular Spectroscopy*, *60*(3), 689-700. https://doi.org/10.1016/S1386-1425(03)00279-8

[15]. Missaoui, F., Trablsi, K., Moufida, K., Ates, A., Mahmoud, A., Boschini, F., & Rhaiem, A. B. (2023). Structural, dielectric and transport properties of $Na_xFe_{1/2}Mn_{1/2}O_2$ (x= 1 and 2/3). *RSC advances*, *13*(26), 17923. DOI: 10.1039/d3ra02570e

[16]. Saroha, R., Gupta, A., & Panwar, A. K. (2017). Electrochemical performances of Li-rich layered-layered Li_2MnO_3-$LiMnO_2$ solid solutions as cathode material for lithium-ion batteries. *Journal of Alloys and Compounds*, *696*, 580-589. https://doi.org/10.1016/j.jallcom.2016.11.199

[17]. Siddiqui, H., Parra, M. R., Qureshi, M. S., Malik, M. M., & Haque, F. Z. (2018). Studies of structural, optical, and electrical properties associated with defects in sodium-doped copper oxide (CuO/Na) nanostructures. *Journal of materials science*, *53*(12), 8826-8843. https://doi.org/10.1007/s10853-018-2179-6

[18]. Singh, S., Tangra, A. K., & Lotey, G. S. (2018). Optical and luminescence properties of β-$NaFeO_2$ nanoparticles. *Electronic Materials Letters*, *14*(5), 594-598. https://doi.org/10.1007/s13391-018-0067-5

[19]. Kumar, N., Parui, S. S., Limbu, S., Mahato, D. K., Tiwari, N., & Chauhan, R. N. (2021). Structural and optical properties of sol–gel derived CuO and Cu_2O nanoparticles. *Materials Today: Proceedings*, *41*, 237-241. https://doi.org/10.1016/j.matpr.2020.08.800

[20]. Durai, L., & Badhulika, S. (2020). Facile synthesis of large area pebble-like β-$NaFeO_2$ perovskite for simultaneous sensing of dopamine, uric acid, xanthine and hypoxanthine in human blood. *Materials Science and Engineering: C*, *109*, 110631. https://doi.org/10.1016/j.msec.2020.110631

[21]. Mathiyalagan, K., Karuppiah, K., Ponnaiah, A., Rengapillai, S., & Marimuthu, S. (2022). Significant role of magnesium substitution in improved performance of layered O3-Na-Mn-Ni-Mg-O cathode material for developing sodium-ion batteries. *International Journal of Energy Research*. https://doi.org/10.1002/er.7864

[22]. Wen, H., & Tanner, P. A. (2015). Optical properties of 3d transition metal ion-doped sodium borosilicate glass. *Journal of Alloys and Compounds*, *625*, 328-335. https://doi.org/10.1016/j.jallcom.2014.11.094

[23]. Vaidhyanathan, B., Kumar, C. P., Rao, J. L., & Rao, K. J. (1998). Spectroscopic investigations of manganese ions in microwave-prepared $NaPO_3$–PbO glasses. *Journal of Physics and Chemistry of Solids*, *59*(1), 121-128. https://doi.org/10.1016/S0022-3697(97)00178-9

[24]. Moustafa, F. A., Fayad, A. M., Ezz-Eldin, F. M., & El-Kashif, I. (2013). Effect of gamma radiation on ultraviolet, visible and infrared studies of NiO, Cr_2O_3 and Fe_2O_3-doped alkali borate glasses. *Journal of Non-CrystallineSolids*, *376*,18. https://doi.org/10.1016/j.jnoncrysol.2013.04.052

[25]. Ravikumar, R. V. S. S. N., Komatsu, R., Ikeda, K., Chandrasekhar, A. V., Ramamoorthy, L., Reddy, B. J., & Rao, P. S. (2003). Spectroscopic studies of copper-doped $ARbB_4O_7$ (A= Na, K) glasses. *Physica B: Condensed Matter*, *334*(3-4), 398-402. https://doi.org/10.1016/S0921-4526(03)00104-2

[26]. Chakradhar, R. S., Murali, A., & Rao, J. L. (1998). Electron paramagnetic resonance and optical absorption studies of Cu^{2+} ions in alkali barium borate glasses. *Journal of Alloys and Compounds*, *265*(1-2), 29-37. https://doi.org/10.1016/S0925-8388(97)00437-4

[27]. Ravikumar, R. V. S. S. N., Komatsu, R., Ikeda, K., Chandrasekhar, A. V., Reddy, B. J., Reddy, Y. P., & Rao, P. S. (2003). EPR and optical studies on transition metal doped $LiRbB_4O_7$ glasses. *Journal of Physics and Chemistry of Solids*, *64*(2), 261-264. https://doi.org/10.1016/S0022-3697(02)00289-5

[28]. Harrabi, D., Hcini, S., Dhahri, J., Wederni, M. A., Alshehri, A. H., Mallah, A., & Bouazizi, M. L. (2022). Study of Structural and Optical Properties of Cu–Cr Substituted Mg–Co Spinel Ferrites for Optoelectronic Applications. *Journal of*

Inorganic and Organometallic Polymers and Materials, 1-14. https://doi.org/10.1007/s10904-022-02484-w

[29]. Wang, J., Zhang, C., Liu, H., McLaughlin, R., Zhai, Y., Vardeny, S. R., & Vardeny, Z. V. (2019). Spin-optoelectronic devices based on hybrid organic-inorganic trihalide perovskites. *Nature communications*, *10*(1), 1-6. https://doi.org/10.1038/s41467-018-07952-x

[30]. Trabelsi, K., Karoui, K., Jomni, F., & Rhaiem, A. B. (2021). Optical and AC conductivity behavior of sodium orthosilicate Na_2CoSiO_4. *Journal of Alloys and Compounds*, *867*, 159099. https://doi.org/10.1016/j.jallcom.2021.159099

[31]. Huang, Y. L., Ying, T. T., Zhao, Y. R., Tang, Y. Z., Tan, Y. H., Li, Q. L., & Wang, F. X. (2023). Zero-Dimensional Sn-Based Enantiomeric Phase Transition Materials with High-Tc and Dielectric Switching. *Chemistry–A European Journal*, e202301499. https://doi.org/10.1002/chem.202301499

[32]. Singh, B., Singh, P., Siddiqui, S., Singh, D., & Gupta, M. (2022). Wastewater treatment using Fe-doped perovskite manganites by photocatalytic degradation of methyl orange, crystal violet and indigo carmine dyes in tungsten bulb/sunlight. *Journal of Rare Earths*. https://doi.org/10.1016/j.jre.2022.09.010

[33]. Geetha, N., Kumar, V. S., & Prakash, D. (2018). Synthesis and characterization of $LaMn_{1-x}Fe_xO_3$ (x= 0, 0.1, 0.2) by coprecipitation route. *J. Phys. Chem. Biophys*, *8*, 1-6. https://DOI: 10.4172/2161-0398.1000273

[34]. Tangra, A. K., & Lotey, G. S. (2021). Synthesis and investigation of structural, optical, magnetic, and biocompatibility properties of nanoferrites $AFeO_2$. *Current Applied Physics*, *27*, 103-116. https://doi.org/10.1016/j.cap.2021.04.011

[35]. Slima, I.B., Karoui, K. & Rhaiem, A.B (2023). Ionic conduction, structural and optical properties of $LiCoO_2$ compound. *Ionics*. https://doi.org/10.1007/s11581-023-04960-w

[36]. Kalthoum, R., Bechir, M. B., & Rhaiem, A. B. (2020). $CH_3NH_3CdCl_3$: A promising new lead-free hybrid organic–inorganic perovskite for photovoltaic applications. *Physica E: Low-dimensional Systems and Nanostructures*, *124*, 114235. https://doi.org/10.1016/j.physe.2020.114235

[37]. Palik, E. D. (Ed.). (1998). *Handbook of optical constants of solids* (Vol. 3). Academic press.

[38]. Kalthoum, R., Bechir, M. B., Rhaiem, A. B., & Dhaou, M. H. (2022). Optical properties of new organic-inorganic hybrid perovskites $(CH_3)_2NH_2CdCl_3$

and$CH_3NH_3CdCl_3$ for solar cell applications. *Optical Materials*, *125*, 112084. https://doi.org/10.1016/j.optmat.2022.112084

[39]. Mahfoudh, N., Karoui, K., & BenRhaiem, A. (2021). Optical studies and dielectric response of $[DMA]_2MCl_4$ (M= Zn and Co) and $[DMA]_2ZnBr_4$. *RSC advances*, *11*(40), 24526-24535. https://doi.org/10.1039/D1RA03652A

[40]. Singh, R. K., Kumar, R., Jain, N., Dash, S. R., Singh, J., & Srivastava, A. (2019). Investigation of optical and dielectric properties of $CsPbI_3$ inorganic lead iodide perovskite thin film. *Journal of the Taiwan Institute of Chemical Engineers*, *96*, 538-542. https://doi.org/10.1016/j.jtice.2018.11.001

[41]. Yan, X., Poxson, D. J., Cho, J., Welser, R. E., Sood, A. K., Kim, J. K., & Schubert, E. F. (2013). Enhanced omnidirectional photovoltaic performance of solar cells using multiple-discrete-layer tailored-and low-refractive index anti-reflection coatings. *Advanced Functional Materials*, *23*(5), 583-590. https://doi.org/10.1002/adfm.201201032

[42]. Abouhaswa, A. S., Rammah, Y. S., Ibrahim, S. E., & El-Hamalawy, A. A. (2018). Structural, optical, and electrical characterization of borate glasses doped with SnO_2. *Journal of Non-Crystalline Solids*, *494*, 59-65. https://doi.org/10.1016/j.jnoncrysol.2018.04.051

[43]. Mguedla, R., Kharrat, A. B. J., Taktak, O., Souissi, H., Kammoun, S., Khirouni, K., & Boujelben, W. (2020). Experimental and theoretical investigations on optical properties of multiferroic $PrCrO_3$ ortho-chromite compound. *Optical Materials*, *101*, 109742. https://doi.org/10.1016/j.optmat.2020.109742

[44]. Ajmi, A., Karoui, K., Khirouni, K., & Rhaiem, A. B. (2019). Optical and dielectric properties of $NaCoPO_4$ in the three phases α, β and γ. *RSC advances*, *9*(26), 14772-14781. https:// DOI: 10.1039/c9ra01558b

[45]. Nageswara Rao, B., Venkateswarlu, M., & Satyanarayana, N. (2014). Electrical and dielectric properties of rare earth oxides coated $LiCoO_2$ particles. *Ionics*, *20*(2), 175-181. https://doi.org/10.1007/s11581-013-0973-3

[46]. Arya, A., & Sharma, A. L. (2019). Dielectric relaxations and transport properties parameter analysis of novel blended solid polymer electrolyte for sodium-ion rechargeable batteries. *Journal of Materials Science*, *54*(9), 7131-7155. https://doi.org/10.1007/s10853-019-03381-3

[47]. Benali, E. M., Benali, A., Bejar, M., Dhahri, E., Graca, M. P. F., Valente, M. A., & Costa, B. F. O. (2020). Effect of annealing temperature on structural, morphological

and dielectric properties of $La_{0.8}Ba_{0.1}Ce_{0.1}FeO_3$ perovskite. *Journal of Materials Science: Materials in Electronics*, *31*(19), 16220-16234. https://doi.org/10.1007/s10854-020-04140-w

[48]. Kalthoum, R., Ben Bechir, M., Ben Rhaiem, A., & Gargouri, M. (2021). $MCdCl_3$ (M= CH_3NH_3,$(CH_3)_2NH_2$): New Hybrid Perovskites with Large Dielectric Constants for Field-Effect Transistors. *Physica Status Solidi (a)*, *218*(24), 2100485. https://doi.org/10.1002/pssa.202100485

[49]. Hastuti, E., Subhan, A., Amonpattaratkit, P., Zainuri, M., & Suasmoro, S. (2021). The effects of Fe-doping on MnO_2: phase transitions, defect structures and its influence on electrical properties. *RSC Advances*, *11*(14), 7808-7823. https://doi.org/10.1039/D0RA10376D

[50]. Mahani, R. M., & Marzouk, S. Y. (2013). AC conductivity and dielectric properties of SiO_2–Na_2O–B_2O_3–Gd_2O_3 glasses. *Journal of Alloys and Compounds*, *579*, 394-400. https://doi.org/10.1016/j.jallcom.2013.05.173

[51]. Murali, N., Margarette, S. J., Rao, V. K., & Veeraiah, V. (2017). Structural, impedance, dielectric and modulus analysis of $LiNi_{1-xy-0.02}Mg_{0.\ 02}Co_xZn_yO_2$ cathode materials for lithium-ion batteries. *Journal of Science: Advanced Materials and Devices*, *2*(2), 233-244. https://doi.org/10.1016/j.jsamd.2017.04.004

[52]. Saha, B. C., Bera, A. K., & Yusuf, S. M. (2021). Mechanism of Na-Ion Conduction in the Highly Efficient Layered Battery Material $Na_2Mn_3O_7$. *ACS Applied Energy Materials*, *4*(6), 6040-6054. https://doi.org/10.1021/acsaem.1c00825

[53]. Costa, L. C., Teixeira, S. S., & Graça, M. (2019, December). Structural, morphologic and dielectric properties of sodium ferrites. In *AIP Conference Proceedings* (Vol. 2196, No. 1, p. 020008). AIP Publishing LLC. https://doi.org/10.1063/1.5140281

[54]. Yi, T. F., Sari, H. M. K., Li, X., Wang, F., Zhu, Y. R., Hu, J., ... & Li, X. (2021). A review of niobium oxides based nanocomposites for lithium-ion batteries, sodium-ion batteries and supercapacitors. *Nano Energy*, *85*, 105955. https://doi.org/10.1016/j.nanoen.2021.105955

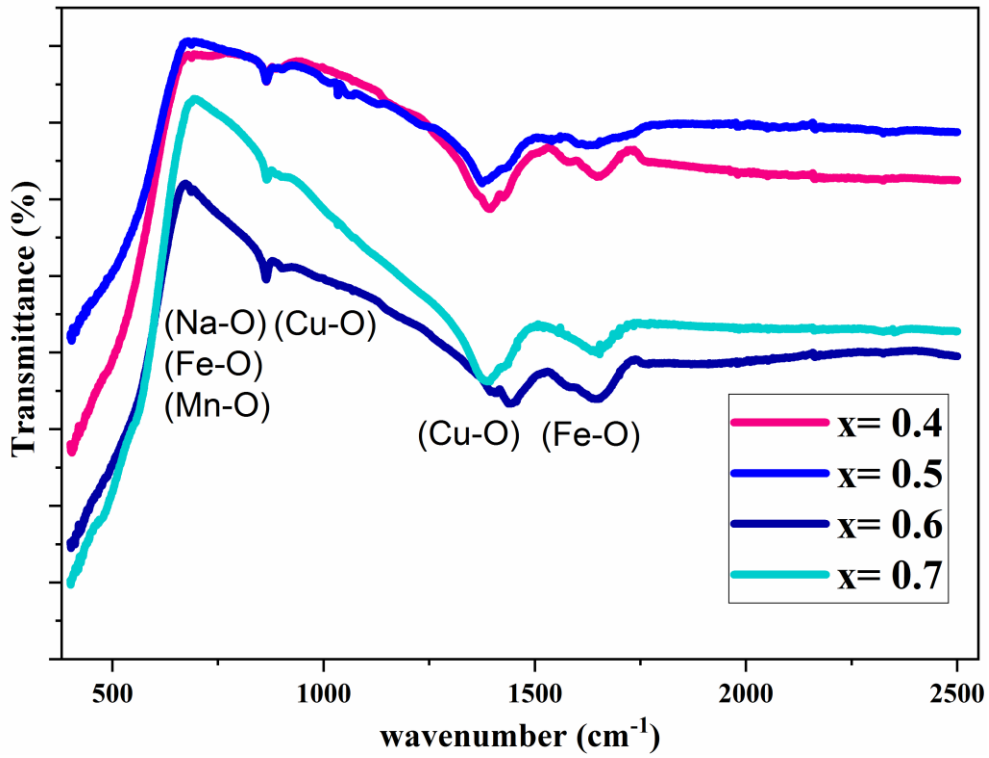

Figure 1: FTIR spectra of pattern associated to $NaCu_{0.2}Fe_{0.8-x}Mn_xO_2$ samples (x= 0.4; 0.5; 0.6; 0.7)

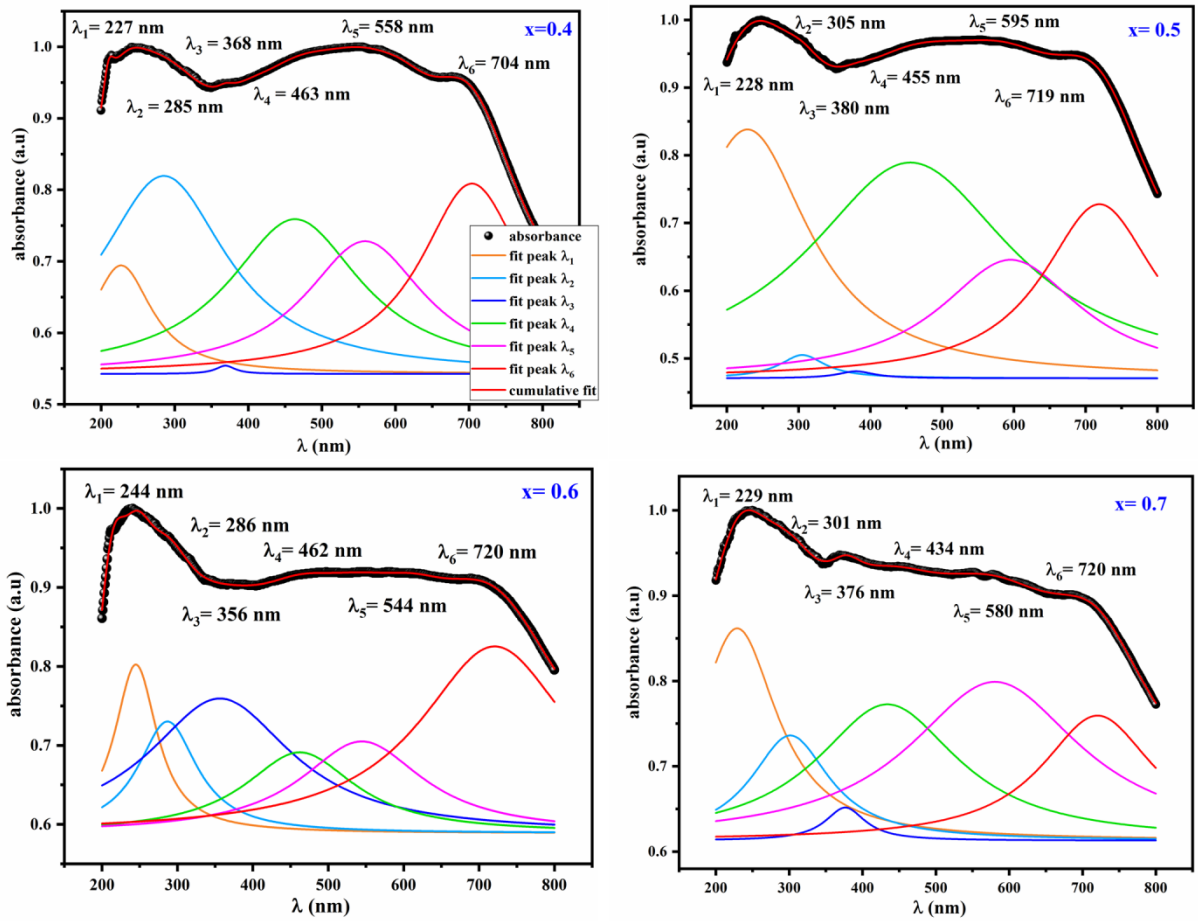

Figure 2: UV-visible absorbance spectra of $NaCu_{0.2}Fe_{0.8-x}Mn_xO_2$ samples (x= 0.4; 0.5; 0.6; 0.7)

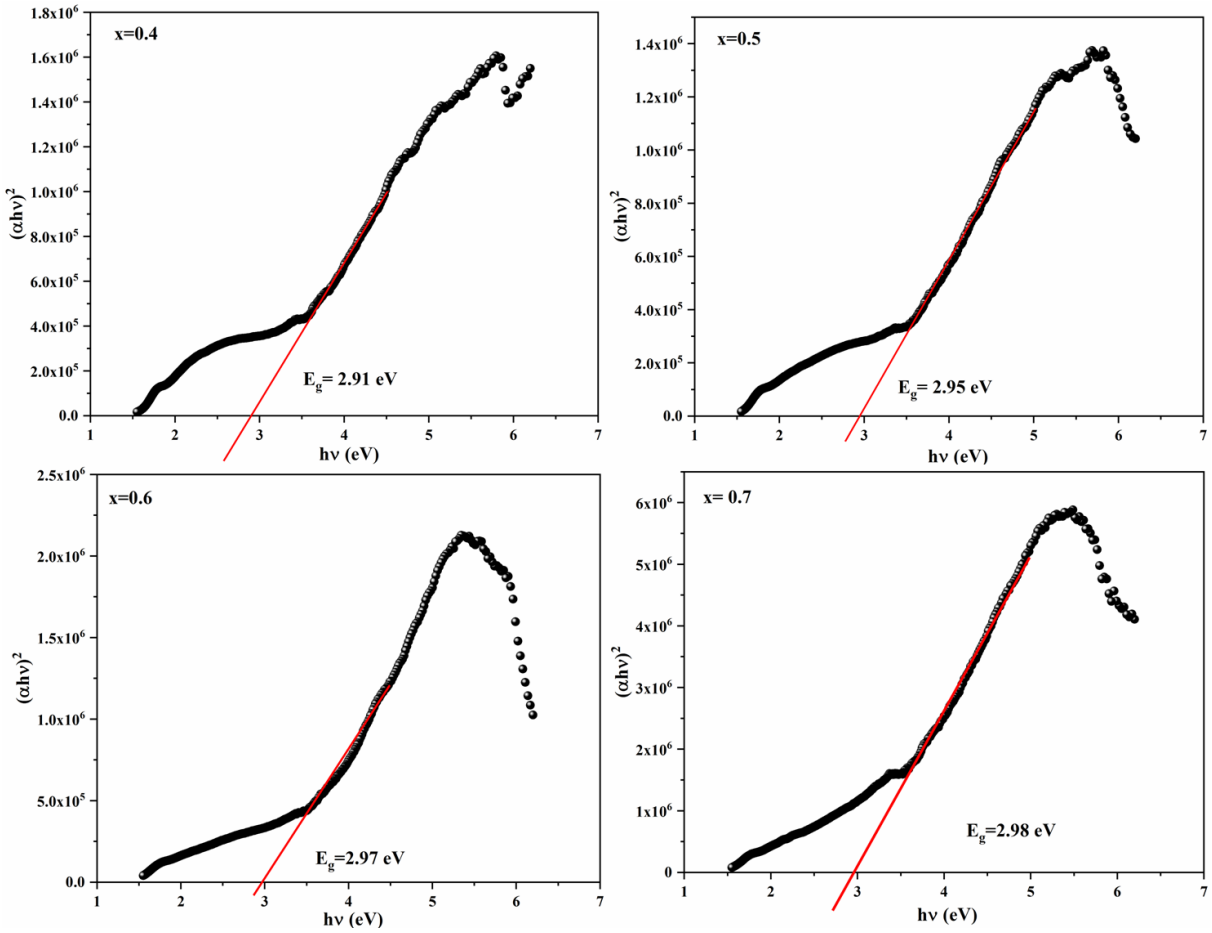

Figure 3: Tauc's plot of $NaCu_{0.2}Fe_{0.8-x}Mn_xO_2$ samples (x= 0.4; 0.5; 0.6; 0.7)

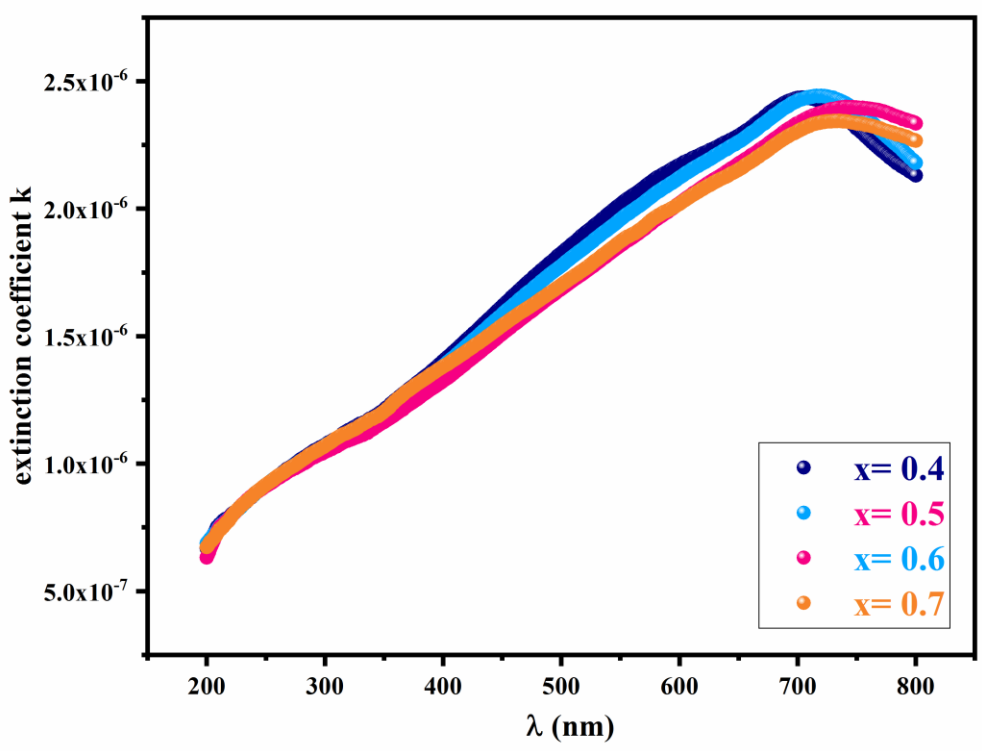

Figure 4 : variation of the extinction coefficient of $NaCu_{0.2}Fe_{0.8-x}Mn_xO_2$ samples (x= 0.4; 0.5; 0.6; 0.7)

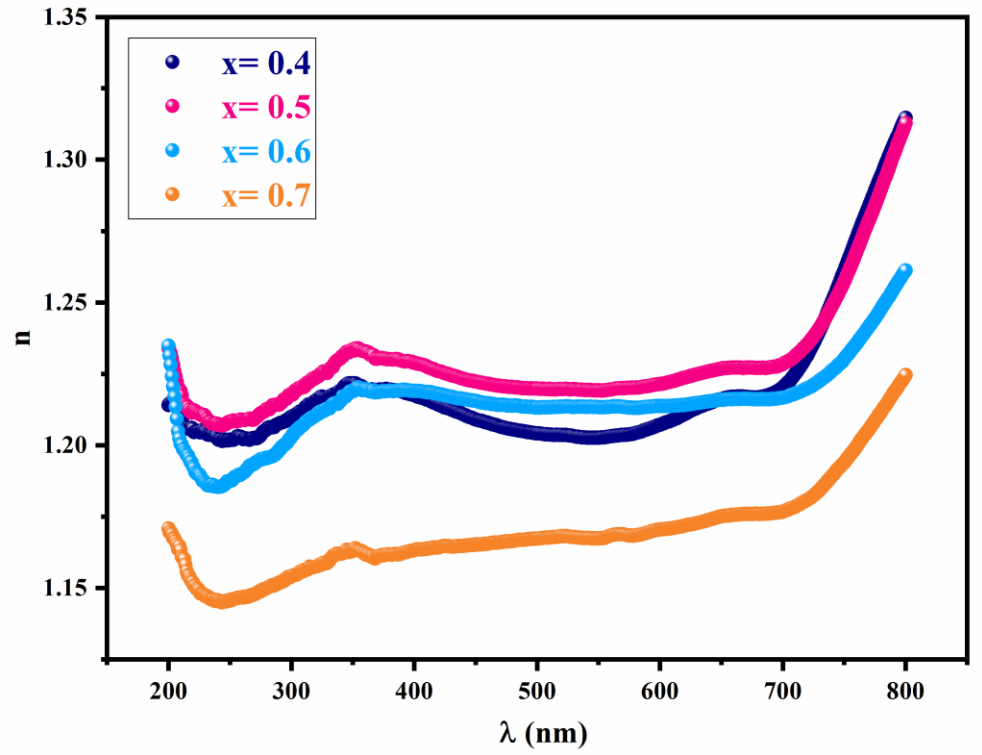

Figure 5 : variation of the refractive index of $NaCu_{0.2}Fe_{0.8-x}Mn_xO_2$ samples (x= 0.4; 0.5; 0.6; 0.7)

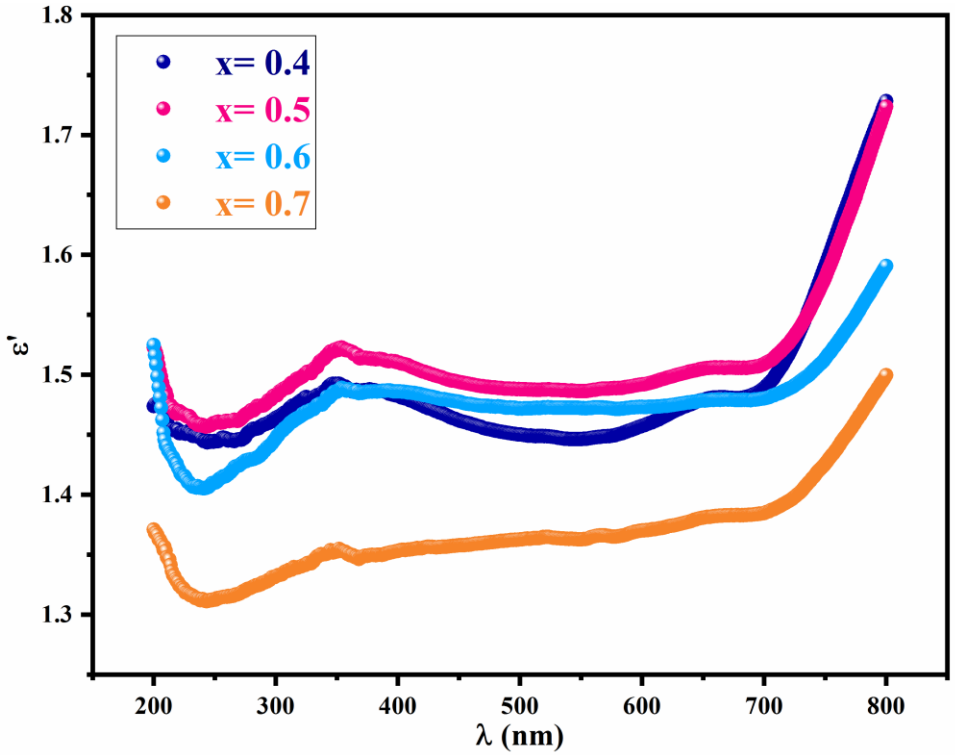

Figure 6 : variation of the real part of the optical dielectric constant of $NaCu_{0.2}Fe_{0.8-x}Mn_xO_2$ samples (x= 0.4; 0.5; 0.6; 0.7)

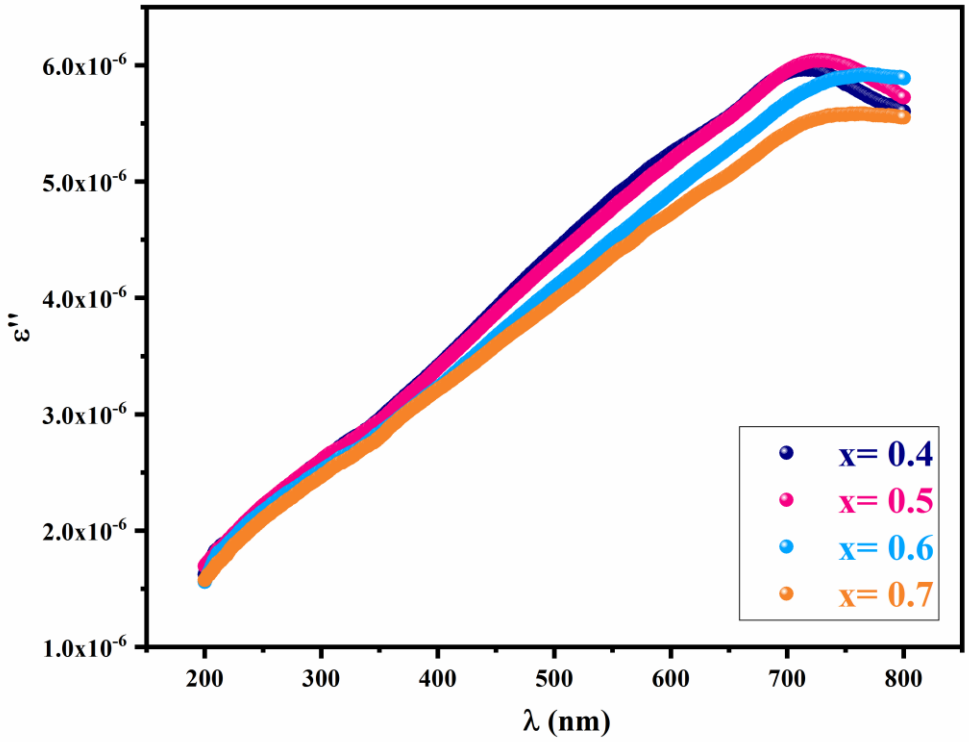

Figure 7 : variation of the imaginary part of the optical dielectric constant of $NaCu_{0.2}Fe_{0.8-x}Mn_xO_2$ samples (x= 0.4; 0.5; 0.6; 0.7)

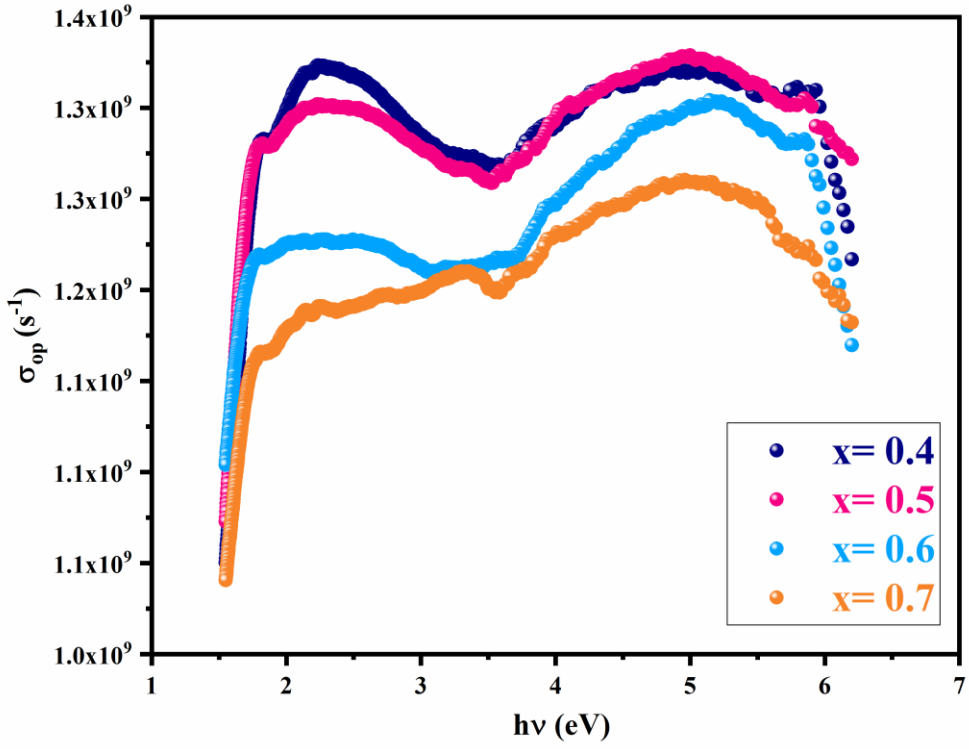

Figure 8 : variation of the optical conductivity of

$NaCu_{0.2}Fe_{0.8-x}Mn_xO_2$ samples (x= 0.4; 0.5; 0.6; 0.7)

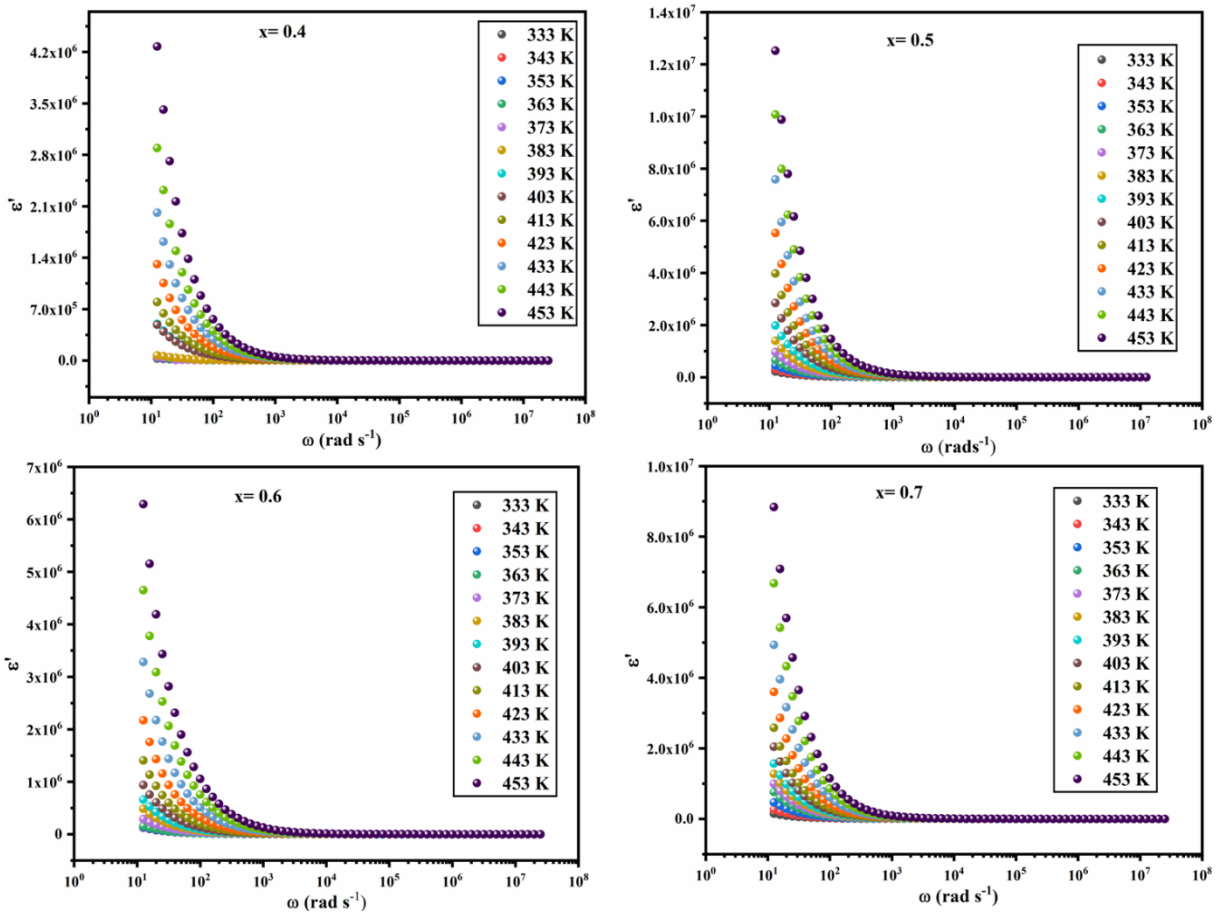

Figure 9 : the frequency dependence of the real part of the dielectric constant ε_{el}' of the $NaCu_{0.2}Fe_{0.8-x}Mn_xO_2$ samples (x= 0.4; 0.5; 0.6; 0.7)

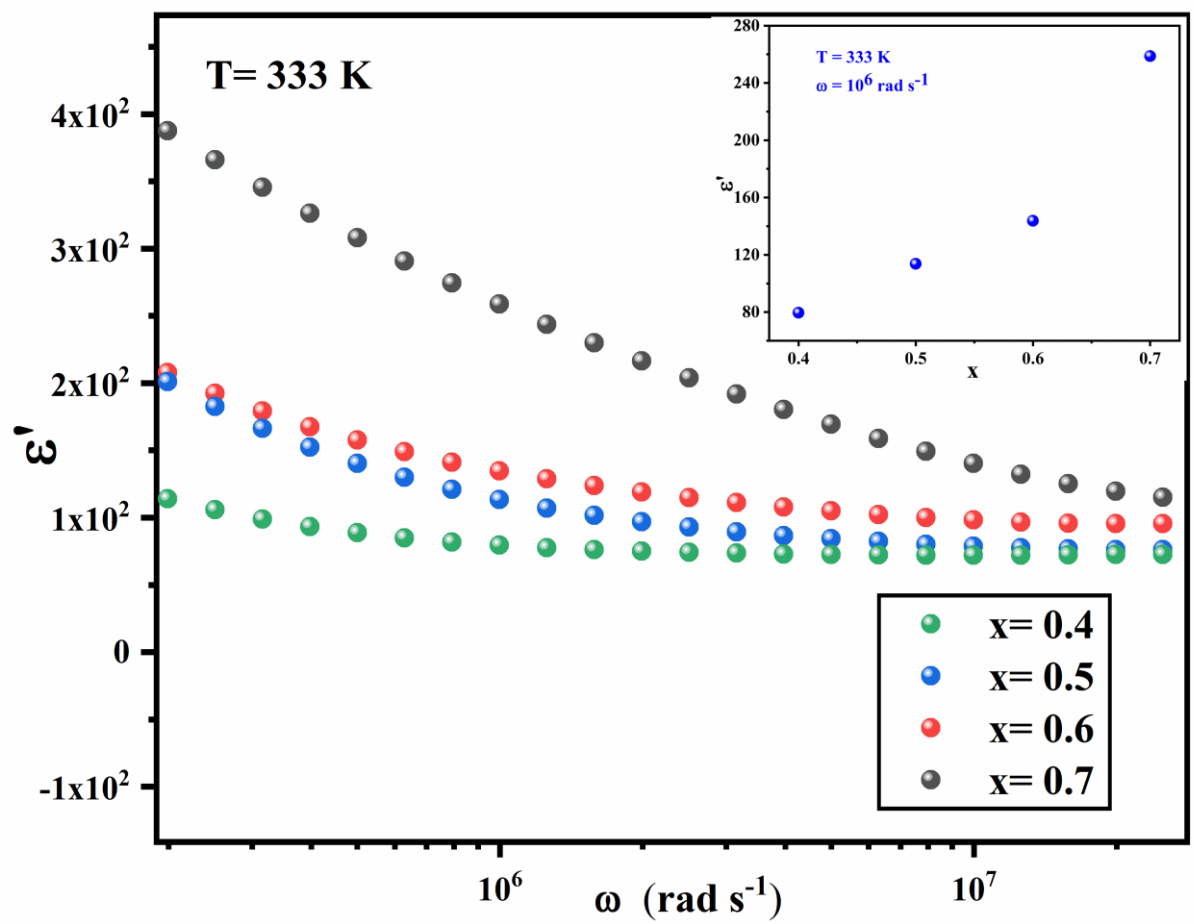

Figure 10: evolution of the real part of the dielectric constant ε_{el}' as a function of Mn percentage of $NaCu_{0.2}Fe_{0.8-x}Mn_xO_2$ samples (x= 0.4; 0.5; 0.6; 0.7) at high frequencies

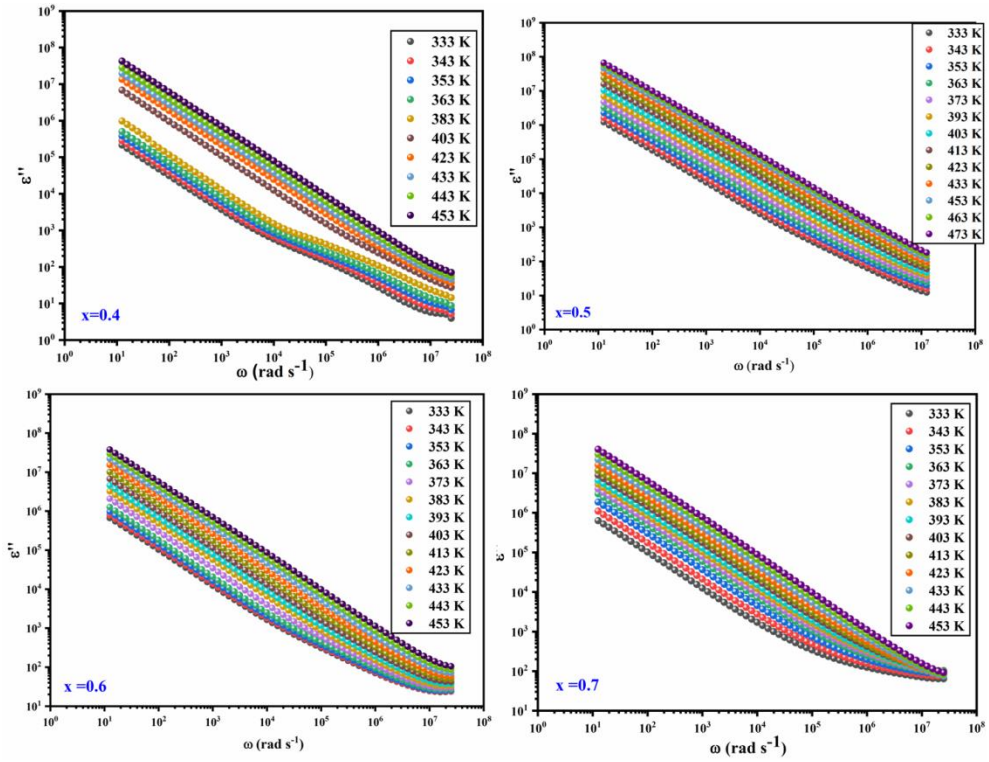

Figure 11 : evolution of the imaginary part of the dielectric permittivity ε_{el}'' against the frequency in log-log plot of the $NaCu_{0.2}Fe_{0.8-x}Mn_xO_2$ samples (x= 0.4; 0.5; 0.6; 0.7)

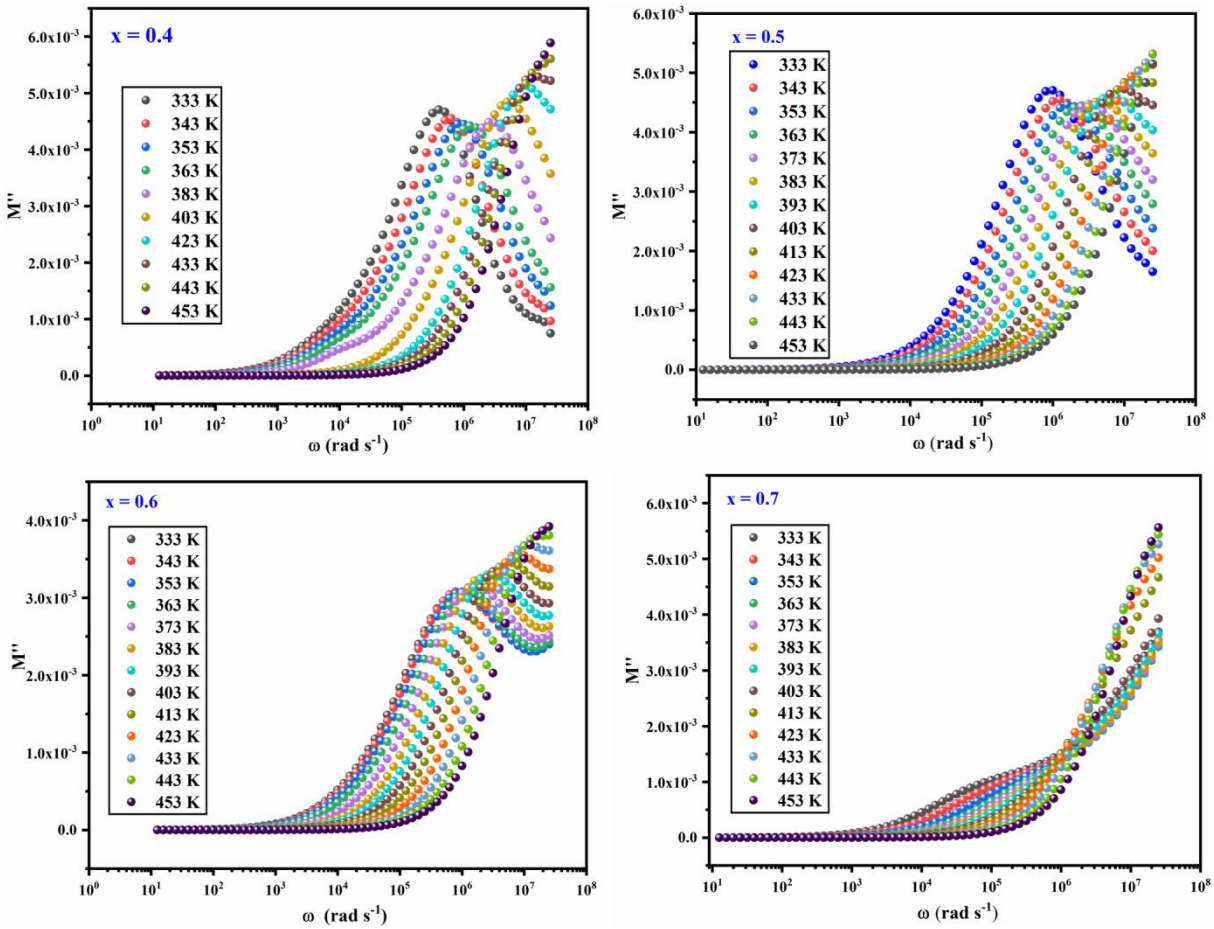

Figure 12: evolution of the imaginary part of modulus **M**" of the $NaCu_{0.2}Fe_{0.8-x}Mn_xO_2$ samples (x= 0.4; 0.5; 0.6; 0.7)

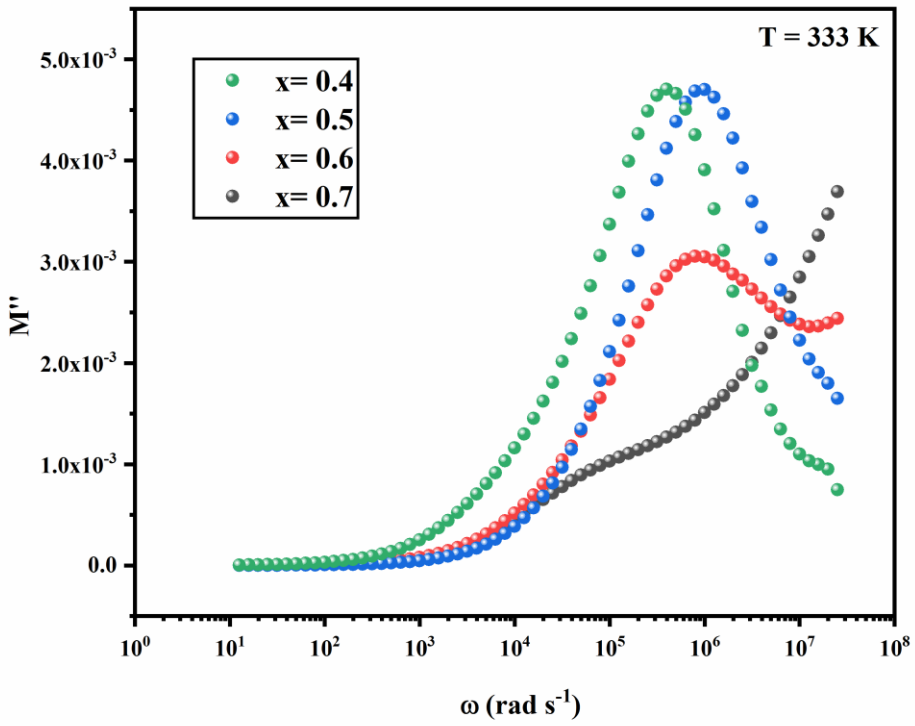

Figure 13: evolution of the imaginary part of modulus **M**" as a function of Mn percentage of $NaCu_{0.2}Fe_{0.8-x}Mn_xO_2$ samples (x= 0.4; 0.5; 0.6; 0.7)

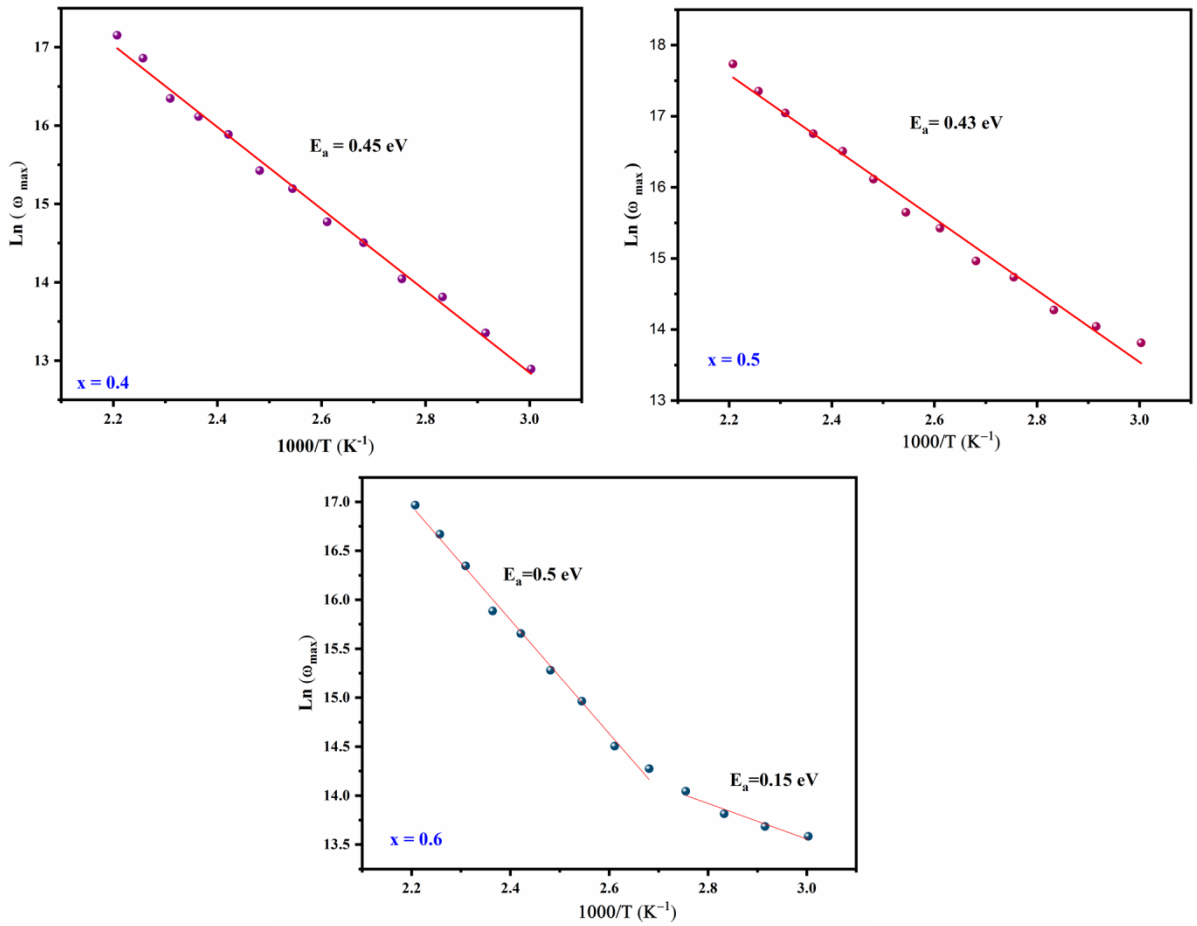

Figure 14: variation of Ln (ω_{max}) vs. the inverse of temperature of $NaCu_{0.2}Fe_{0.8-x}Mn_xO_2$ samples (x= 0.4; 0.5; 0.6)

Table 1 : The vibration peaks appeared from FTIR spectra of $NaCu_{0.2}Fe_{0.8-x}Mn_xO_2$ samples (x= 0.4; 0.5; 0.6; 0.7).

	x=0.4	**x=0.5**	**x=0.6**	**x=0.7**		**Ref**
peak1	687	687	687	-	Stretching Na-O/Fe-O/ Mn-O/Na-Cu-O Cu-O vibration	[14-16]
peak 2	865	865	863	863		
peak 3	-	902	902	-	Bonding Fe-O-Fe Stretching Cu-O	[18-19]
peak 4	-	1034	-	1034	Stretching and bonding O-Fe-O	[20]
peak 5	1385	1375	1442	1390	Na-Cu-O vibration	[17]
peak 6	1651	1624	1651	1653	Bonding O-H	[21]

Table 2 : Gap energy of $NaCu_{0.2}Fe_{0.8-x}Mn_xO_2$ samples (x= 0.4; 0.5; 0.6; 0.7)

x	**E_g (eV)**
0.4	2.91
0.5	2.95
0.6	2.97
0.7	2.98

Table 3 : activation energy of $NaCu_{0.2}Fe_{0.8-x}Mn_xO_2$ samples (x= 0.4; 0.5; 0.6; 0.7)

x	E_a (eV)
0.4	0.45
0.5	0.43
0.6	0.5

Supporting information

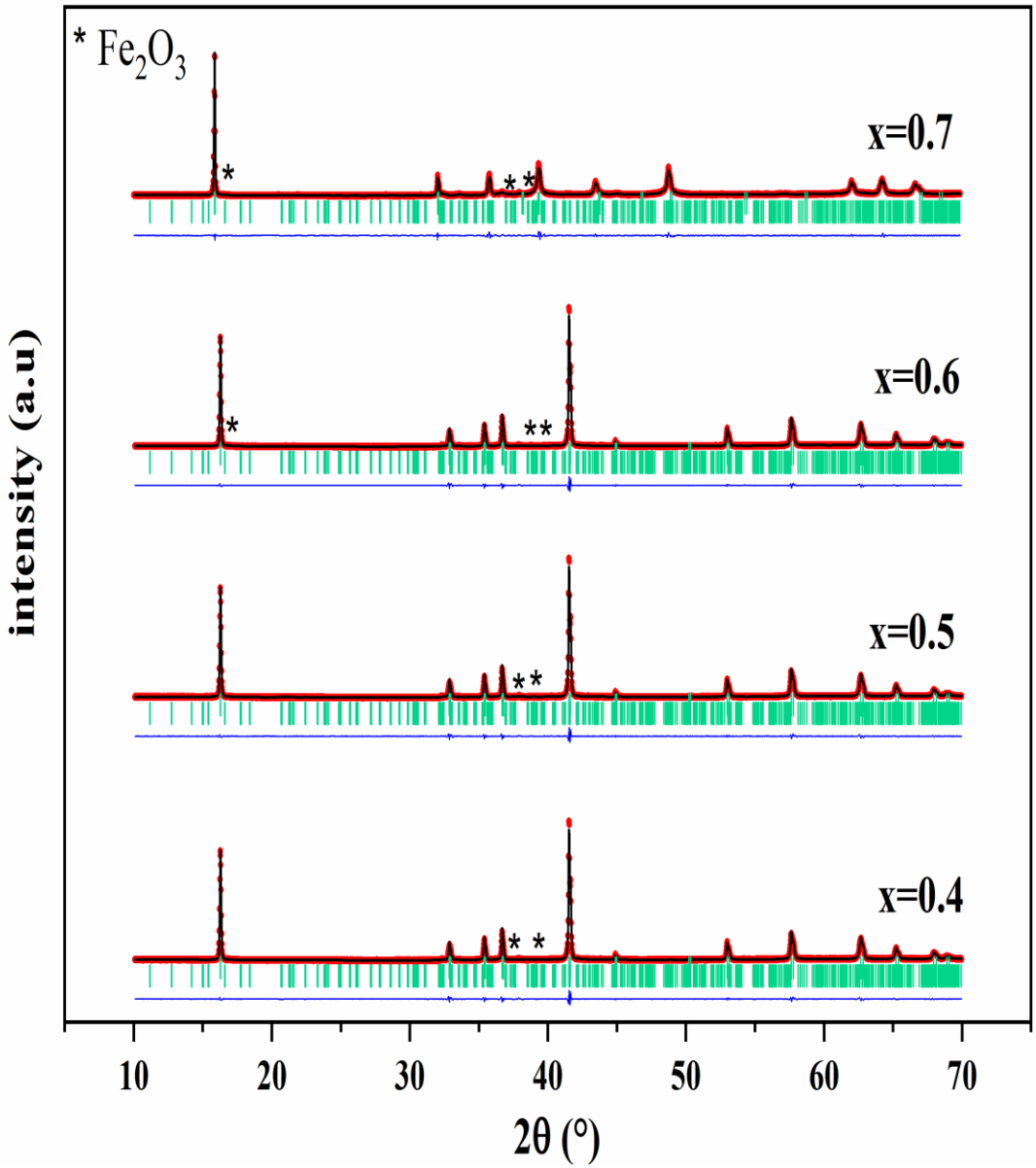

Figure S15 : XRD pattern associated to $NaCu_{0.2}Fe_{0.8-x}Mn_xO_2$ samples (x= 0.4; 0.5; 0.6; 0.7) [1]

Fig. S1 exhibits the X-Ray Diffraction patterns of $NaCu_{0.2}Fe_{0.8-x}Mn_xO_2$ compounds (x= 0.4; 0.5; 0.6; 0.7). The structure refinement by the Rietveld method using FullProf software confirmed that the samples crystallize in the hexagonal system and are indexed to the R-3m space group and we detect some trace of Fe_2O_3. The cell parameters and the fit criteria are plotted in table S1.

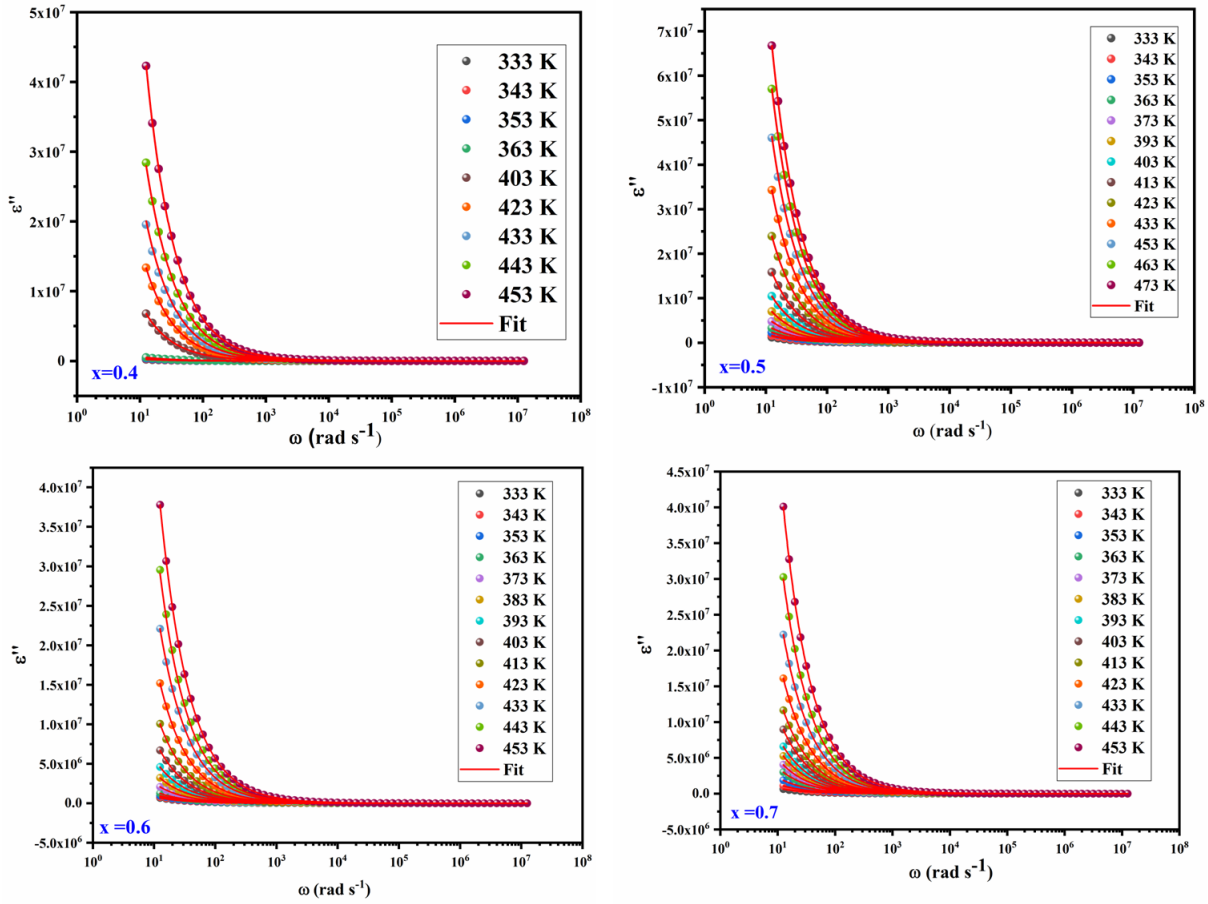

Figure S16 : Fit of the imaginary part of the dielectric permittivity **ε"** against the frequency using cole-cole model of the $NaCu_{0.2}Fe_{0.8-x}Mn_xO_2$ samples (x= 0.4; 0.5; 0.6; 0.7)

Table S4 : System: hexagonal, space group: R-3m **[1]**

x	a(Å)	c(Å)	χ^2	R_p	R_{wp}	R_{exp}
0.4	2.9627(1)	16.3411 (7)	3.77	8.84	8.48	4.37
0.5	2.9389(1)	16.5208 (11)	2.42	9.67	8.08	5.20
0.6	2.8107 (2)	16.8160 (5)	5.28	11.8	11.6	5.04
0.7	2.7326 (5)	16.7607 (4)	5.51	11.1	11.7	5.51

Tableau S5 : σ_{dc} conductivity obtained from the adjustment of the imaginary part of the dielectric permittivity **ε"** against the frequency of the $NaCu_{0.2}Fe_{0.8-x}Mn_xO_2$ samples (x= 0.4; 0.5; 0.6; 0.7)

	X= 0.4	**X= 0.5**	**X= 0.6**	**X= 0.7**
	(Ω cm)$^{-1}$	**(Ω cm)$^{-1}$**	**(Ω cm)$^{-1}$**	**(Ω cm)$^{-1}$**
333 K	9.028.10^{-6}	7.51.10^{-6}	3.12.10^{-5}	2.94.10^{-5}
343 K	1.91.10^{-5}	9.89.10^{-6}	3.80.10^{-5}	4.83.10^{-5}
353 K	2.022.1	2.2.10^{-5}	4.46.10^{-5}	8.21.10^{-5}

	0^{-5}		^{5}	^{5}	
363 K	$2.36.10^{-5}$	$6.68.10^{-5}$	$6.48.10^{-6}$	$1.43.10^{-4}$	
403 K	$3.32.10^{-4}$	$5.01.10^{-4}$	$3.58.10^{-4}$	$4.97.10^{-4}$	
423 K	$4.71.10^{-4}$	$1.15.10^{-3}$	$8.44.10^{-4}$	$8.32.10^{-4}$	
433 K	$6.66.10^{-4}$	$2.28.10^{-3}$	$9.23.10^{-4}$	$1.01.10^{-3}$	
443 K	$8.33.10^{-4}$	$2.53.10^{-3}$	$1.20.10^{-3}$	$2.20.10^{-3}$	
453 K	$1.56.10^{-3}$	$3.31.10^{-3}$	$1.38.10^{-3}$	$2.41.10^{-3}$	

References:

[1]. Slima, I. B., Karoui, K., Mahmoud, A., Boschini, F., & Rhaiem, A. B. (2022). Effects of Mn doping on structural properties and conduction mechanism of $NaCu_{0.2}Fe_{0.8-x}Mn_xO_2$ (x= 0.4; 0.5; 0.6; 0.7) materials. *Journal of Alloys and Compounds*, *920*, 166002. https://doi.org/10.1016/j.jallcom.2022.166002.